Oceanic Isopycnal Slope Spectra. Part I: Internal Waves

JODY M. KLYMAK

Scripps Institution of Oceanography, University of California, San Diego, La Jolla, California

JAMES N. MOUM

College of Oceanic and Atmospheric Sciences, Oregon State University, Corvallis, Oregon

ABSTRACT

Horizontal tow measurements of internal waves are rare and have been largely supplanted in recent decades by vertical profile measurements. Here, estimates of isotherm displacements and turbulence dissipation rate from a towed vehicle deployed near Hawaii are presented. The displacement data are interpreted in terms of horizontal wavenumber spectra of isopycnal slope. The spectra span scales from 5 km to 0.1 m, encompassing both internal waves and turbulence. The turbulence subrange is identified using a standard turbulence fit, and the rest of the motions are deemed to be internal waves. The remaining subrange has a slightly red slope ($\phi \sim k_x^{-1/2}$) and vertical coherences compatible with internal waves, in agreement with previous towed measurements. However, spectral amplitudes in the internal wave subrange exhibit surprisingly little variation despite a four-order-of-magnitude change in turbulence dissipation rate observed at the site. The shape and amplitude of the horizontal spectra are shown to be consistent with observations and models of vertical internal wave spectra that consist of two subranges: a "linear" subrange ($\phi \sim k_z^0$) and a red "saturated" subrange ($\phi \sim k_z^{-1}$). These two subranges are blurred in the transformation to horizontal spectra, yielding slopes close to those observed. The saturated subrange does not admit amplitude variations in the spectra yet is an important component of the measured horizontal spectra, explaining the poor correspondence with the dissipation rate.

1. Introduction

At superinertial frequencies, velocities and isopycnal displacements in the ocean have contributions from internal waves and turbulence. These small-scale motions are believed to be responsible, either directly or indirectly, for most of the irreversible mixing of momentum and tracers in the interior of the ocean. The mixing is typically thought of as a cascade of energy from large-scale internal wave generating processes such as the wind (i.e., Gregg et al. 1986; Hebert and Moum 1994; D'Asaro 1995; Alford and Gregg 2001), and the tides (i.e., St. Laurent and Garrett 2002; Rudnick et al. 2003; Polzin 2004), through an internal wave continuum to turbulence. Thus, in most conceptual models, turbulence and internal waves are directly coupled.

Wavenumber spectra are often used to statistically characterize internal wave and turbulent motions. Different physics dominate at different wavenumbers, so spectra are divided into subranges. The most general division is between turbulence at small scales and nonturbulent motions, usually internal waves, at larger scales (Fig. 1). In this paper, we discuss gradients of vertical isopycnal displacement ζ; in profiles vertical gradients are referred to as *strain* (ζ_z), while horizontal tow gradients are the *slope* of isopycnals (ζ_x). Gradient spectra are blue at high wavenumbers where turbulence dominates. They are slightly red or white where internal waves dominate.

Our understanding of the internal wave field is primarily empirical, with various fits to frequency and wavenumber spectra (a model hereinafter referred to as GM81; Cairns and Williams 1976; Munk 1981; Gregg and Kunze 1991). These fits have proven robust in the open ocean and are used routinely to quantify internal wave energy and turbulence levels (Gregg 1989; Kunze and Sanford 1996; Nagasawa et al. 2002; Naveira Ga-

Corresponding author address: J. Klymak, School of Earth and Ocean Sciences, University of Victoria, P.O. Box 3055, STN CSC, Victoria, BC V8W 3P6, Canada.
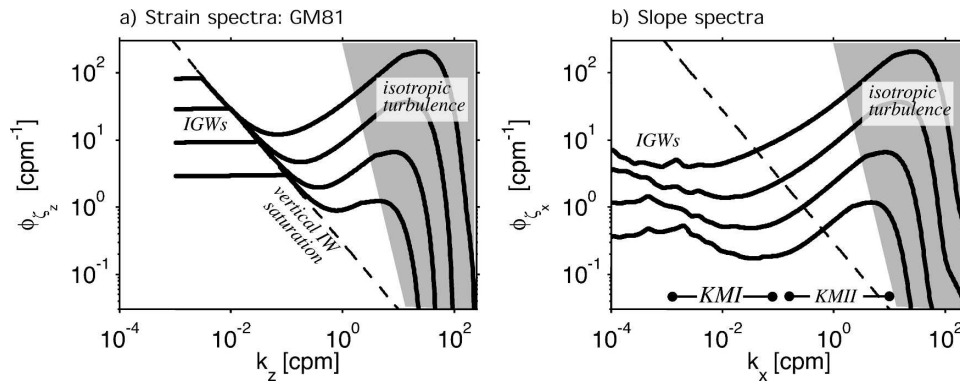E-mail: jklymak@uvic.ca

FIG. 1. (a) GM81 strain spectra with saturated internal wave subrange and turbulence for four different energy levels and their corresponding turbulence levels assuming $\varepsilon \sim E^2$. After D'Asaro and Lien (2000) except turbulence is added to the internal wave spectrum rather than intersecting them with a sharp change of slope. (b) Slope spectra in the same wave and turbulence fields as calculated in the text (section 6). The same dashed line as in (a) is shown for reference. (The slightly jagged nature of these spectra is due to representing the vertical spectra as discrete modes rather than continuous wavenumbers.) This paper is concerned with the low-wavenumber portion of the horizontal spectra.

rabato et al. 2004; Kunze et al. 2006). The wavenumber shape is derived from vertical profiling measurements of shear and strain (Gargett et al. 1981; Sherman and Pinkel 1991; Gregg et al. 1993; Polzin et al. 1995). Formally, GM81 only admits one subrange, but all of these studies demonstrate that vertical spectra consist of two distinct subranges. The first is white at low wavenumbers, transitioning to a second red subrange at $k_z \gtrsim 0.1$ cpm (Fig. 1a). As energy levels increase, the transition occurs at lower wavenumbers, approximately conforming to a critical Froude number criteria. The physics of the second subrange are poorly understood, but are believed to be highly nonlinear (D'Asaro and Lien 2000; Hines 1991a,b). For simplicity, we refer to this as a "saturated" subrange following the terminology used in the atmospheric internal wave literature where a similar phenomena is found (Smith et al. 1987; Gardner 1996).

This paper presents horizontal spectra of isopycnal slopes collected near the Hawaiian Ridge. The bulk of the towed spectra cited above were published before the presence of a second saturated subrange was recognized. Like the vertical measurements, these studies found relatively universal spectra in the open ocean and fit these spectra to a single subrange. The best fit was $\phi_{\zeta_x} \sim k_x^{-0.5}$ with a whitening at low wavenumbers (McKean and Ewart 1974; Katz 1975; Katz and Briscoe 1979; Dugan et al. 1986). This work led to an older version of the Garrett–Munk fit (hereinafter referred to as GM75; Garrett and Munk 1975). If we assume one subrange, our horizontal spectra are also consistent with GM75. Below, we calculate the shape of the two-subrange GM81 model in horizontal tows and demon-

strate that the saturated subrange strongly influences the towed spectra.

A brief review of the expected motions (section 2) is followed by a description of our instruments and measurement site (section 3). Isopycnal slope spectra are presented (section 4) both in raw and dissipation-binned form. Our interpretation of these spectra (section 5) briefly touches on the turbulent high-wavenumber subrange (discussed in detail by Klymak and Moum 2007, hereinafter Part II) and then focuses on the low wavenumbers. The low-wavenumber subrange of the observed spectra is only weakly correlated to the turbulence dissipation rate. This, and the apparent inconsistency with strain spectra, leads us to reexamine how to model internal wave slope spectra (section 6). A short discussion and summary follow (section 7).

2. A brief review of spectral subranges

Our spectra are formed from the horizontal gradient of vertical isopycnal displacement (ζ_x). This is related to more often presented temperature variance spectra (ϕ_T) by

$$\phi_{\zeta_x}(k_x) = (2\pi k_x)^2 \left\langle \frac{dT}{dz} \right\rangle^{-2} \phi_T \, [\text{cpm}^{-1}], \qquad (1)$$

where dT/dz is the background vertical temperature gradient and k_x is horizontal wavenumber (cpm). For vertical profilers the corresponding along-measurement gradient of displacement ζ_z is the vertical *strain*. In the cases in which the measurement direction is not specified, we generically refer to *gradient* spectra. Our mea-

surements span both turbulent and internal waves physics, so we discuss the subranges in turn.

a. Internal wave subranges

At large scales, motions are usually dominated by internal waves. They are frequently modeled using an empirical formalism that assumes the waves are separable in vertical wavenumber (k_z) and frequency (ω) (Garrett and Munk 1972):

$$E_{IW}(\omega, k_z) = E B(\omega) A(k_z). \tag{2}$$

Here E is a dimensionless energy level parameter, $B(\omega)$ is a "universal" fit to the frequency content of motions between f and N, and $A(k_z)$ is a universal fit of the wavenumber content.

This spectrum is converted to a dimensional spectrum of isopycnal displacement (ζ) by including a frequency-dependent function:

$$\phi_\zeta(\omega, k_z) = E\overline{Z}^2(\omega)B(\omega)A(k_z), \tag{3}$$

where $\overline{Z}^2$ is the variance of vertical displacements:

$$\overline{Z}^2(\omega) = \frac{b^2 N_0}{N}\frac{\omega^2 - f^2}{\omega^2}, \tag{4}$$

where $b = 1300$ m is the decay scale of the stratification from its value at 1000 m, $N_0 = 5.2 \times 10^{-3}$ s^{-1}, and f is the Coriolis frequency (Garrett and Munk 1972); formally, these parameters should be matched to the local environment (Levine 2002). These spectra are red. Gradient spectra are whitened. The strain spectrum is

$$\phi_{\zeta_z}(\omega, k_z) = (2\pi k_z)^2 E\overline{Z}^2(\omega)B(\omega)A(k_z) \tag{5}$$

and the slope spectrum is

$$\phi_{\zeta_x}(\omega, k_x) = (2\pi k_x)^2 E\overline{Z}^2(\omega)B(\omega)A(k_x). \tag{6}$$

The frequency content of the wave field is modeled as

$$B(\omega) = \frac{2}{\pi}\frac{f}{\omega}(\omega^2 - f^2)^{-1/2}, \tag{7}$$

for $f < \omega < N$. This form ignores the presence of tidal peaks and subtidal whitening often found in real observations (Levine 2002).

In wavenumbers, the single-subrange spectra are fit to a single power law, modified by a bandwidth parameter, k_*, so that the spectra roll off at low wavenumbers (Munk 1981; Gregg and Kunze l991):

$$A(k_z) = A_1(k_z^2 + k_*^2)^{-n/2}, \tag{8}$$

where A_1 is a constant so that $\int A(k_z)\, dk_z = 1$ when integrated over all wavenumbers. This form has been applied to both vertical and horizontal measurements.[1] Horizontal and vertical spectra are related through the linear dispersion relation:

$$\omega^2 = \frac{N^2 k_H^2 + f^2 k_z^2}{k_H^2 + k_z^2}, \tag{9}$$

where $k_H^2 = k_x^2 + k_y^2$ is the total horizontal wavenumber. Horizontal measurements are made in a single wavenumber direction, complicating comparisons between horizontal and vertical spectra with an additional geometric transformation.

A saturated subrange is found in vertical measurements with a red spectrum above a cutoff wavenumber k_c:

$$A(k_z) = A(k_c)\frac{k_c}{k_z} \quad \text{for} \quad k_z > k_c. \tag{10}$$

The cutoff occurs at lower wavenumbers as the internal wave energy level increases, usually calculated from the normalized shear spectrum:

$$\frac{1}{N_0^2}\int_0^{k_c} \phi_{U_z}\, dk_z \approx 0.7, \tag{11}$$

where N_0 is the background buoyancy frequency (Gregg et al. 1993). Thus, for strain spectra, the model has a white subrange for $k_z < k_c$ and a k_z^{-1} slope for $k_z > k_c$ (Fig. 1a).

The effect of this second subrange on horizontal spectral shapes has not been computed nor compared to data before. In the special case where there is no high-k_z roll off, and thus only one subrange, horizontal spectra have the same slope as vertical spectra. Historically this has been assumed, and the slope of the spectra has been determined from horizontal and vertical spectra interchangeably (GM75). Below, we show that this is not possible for two-subrange spectra and that horizontal spectra will have curvature and a slope in a continuum between k_x^0 and k_x^{-1}. The saturated subrange in the vertical also yields a weak amplitude dependence of the horizontal spectra on internal wave energy level. The calculated horizontal spectra roughly agree with the data (McKean and Ewart 1974; Katz 1975; Katz and Briscoe 1979; Dugan et al. 1986).

b. Turbulence subrange

At smaller scales, temperature and velocity fluctuations are dominated by turbulence. Microstructure gradients in the ocean are modeled as isotropic, homogenous, three-dimensional turbulence (Gargett 1985), al-

---

[1] A slightly different form is also used: $A(k_z) = A_2(k_z + k_*)^{-n}$. The data discussed here cannot distinguish between forms.

lowing comparison with laboratory and theoretical work (Batchelor 1959). For this paper, the turbulent portion of the spectrum is removed by fitting to a model

$$\phi_{\zeta_x}^{\text{Turb}} = 2\pi\chi_\zeta[C_T\varepsilon^{-1/3}(2\pi k_x)^{1/3} + q\nu^{1/2}\varepsilon^{-1/2}2\pi k_x][(\text{cpm})^{-1}],$$
(12)

where k_x is the horizontal wavenumber in cycles per meter, ε the turbulence dissipation rate, χ_ζ is an amplitude, $C_T \approx 0.44$ and $q \approx 2.3$ are constants, and ν is the viscocity of seawater. The details of this subrange are dealt with in Part II.

Internal wave and turbulence spectral subranges overlap at intermediate wavenumbers with the cross-over wavenumber depending on their relative amplitudes. Part II advocates that turbulence and internal wave spectra should be added, as sketched in Fig. 1. This serves to whiten the spectra at intermediate wave-number ranges.

3. Instrumentation and experiment site

Our measurements were obtained with Marlin, a towed vehicle, detailed in Moum et al. (2002) and Klymak et al. (2006) (Fig. 2). A 0.680-in. hydrographic wire is deployed with a 1500-kg depressor weight at the end. Marlin is attached to this weight via a 200-m-long cable that takes up strain in elastic cords, damping vibrations caused by strumming of the hydrographic wire. Marlin flies 20–50 m below this weight. Tow speeds were approximately 1 m s^{-1} with variations in the speed and currents inducing small altitude variations in Marlin. The cable and depressor damped out ship motions shorter than 20 min.

The data were collected in the Kauai Channel between Oahu and Kauai as part of the Hawaii Ocean Mixing Experiment (HOME; Fig. 3). Sampling consisted of cross-ridge runs made at approximately 700-m depth, and a dogleg pattern that approached the ridge and then turned northwest following the 3000-m isobath. Doglegs were made at 700, 1800, 2400, and 3000 m (Klymak et al. 2006).

Marlin was equipped with a microstructure suite that measured small-scale velocity gradients, conductivity, temperature, and pressure on the nose, and a temperature sensor on a fin that protruded beneath the body (Fig. 2). The depressor weight was equipped with a SeaBird Seacat CTD (conductivity–temperature–depth). Example data are shown in Fig. 4. Here, Marlin is transiting from south of the ridge to the north, over the ridge ($x = 0$ km; Fig. 4b). Along its path, Marlin measures temperature (Fig. 4a), its depth (Fig. 4b), and turbulent dissipation ε (Fig. 4d). We calculate isotherm
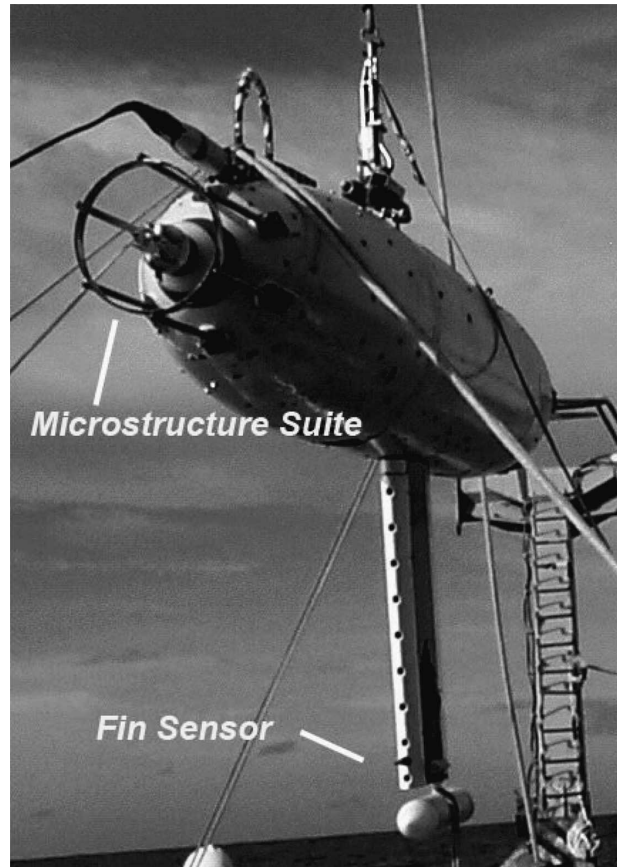

FIG. 2. Marlin deployment of October 2002. The microstructure suite discussed in this paper is on the nose surrounded by a probe guard. The fin sensor is 1.16 m below and 1.9 m aft of the nose sensors. Marlin is buoyed so that the tow cable, seen hanging above the microstructure suite, leads upward toward the depressor weight so that the sensors pass through undisturbed water.

displacement (Fig. 4c) in order to diagnose the internal wave field.

The experiment site exhibited strong variability in internal wave energy and turbulence (Fig. 4). The 5-km bins of ε decreased by two orders of magnitude 60 km away from the ridge (Klymak et al. 2006); individual 5-km averages varied by four orders of magnitude. There was strong variability on smaller horizontal scales as well (Fig. 4d represents 24-s averages), which appears to be correlated to variability in the temperature signal (Fig. 4a).

a. Dissipation measurements

Turbulent dissipation rate ε was calculated from the output of shear foil probes by standard methods (Moum et al. 1995). In weak turbulence, the dissipation measurements are contaminated by vehicle vibration, which was diagnosed using accelerometers in the nose
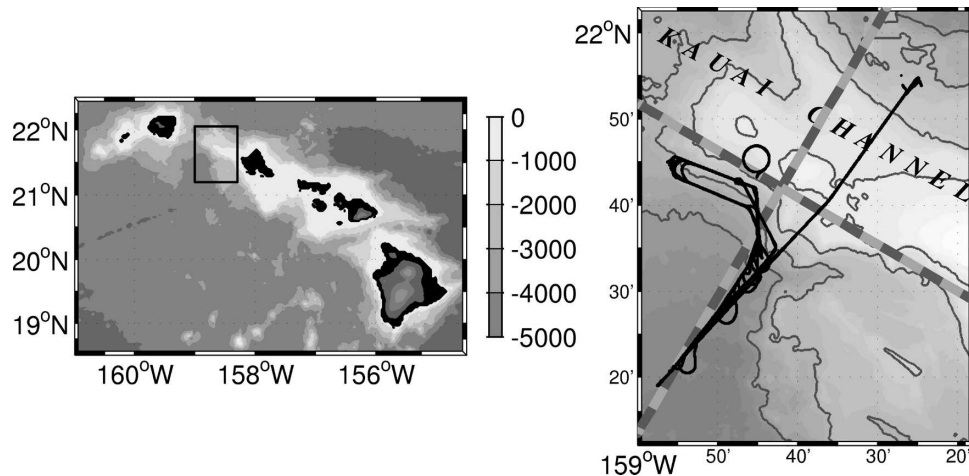
FIG. 3. The Kauai Channel study site between Kauai and Oahu in the Hawaiian Islands. Scale bars define along- and across-ridge axes with 5-km increments in alternating shades of gray. Marlin tracks are shown in black.

of the microstructure package (Levine and Lueck 1999); vibration signals coherent with the shear probe signals were removed and variance computed to get the dissipation rate. If more than one-half of the variance was removed, the calculated dissipation rate was assumed to be dominated by noise and set to $\varepsilon = 10^{-11}$ $m^2 \, s^{-3}$. For the data discussed here, the noise level was $\varepsilon \approx 3 \times 10^{-10} \, m^2 \, s^{-3}$.

b. High-resolution temperature calculation

Temperature was measured using FP07 thermistors on Marlin's nose. The temperature signal was sampled at 39.0625 Hz and differentiated with a time constant of 1.29 s; the differentiated signal was sampled at 156.25 Hz. The resolution of the temperature signal is limited by the sensor's time response and bit noise at high frequencies, whereas an integral of the differentiated signal drifts (slightly) at low frequencies. The two signals were combined in the time domain, following Mudge and Lueck (1994), using a crossover frequency of $\Omega_c = 0.24$ Hz.

c. Relating temperature to displacement

Displacement is calculated relative to a cruise-mean temperature profile (Lee et al. 2006). We define $Z_0(T)$ as the inversion of the mean temperature profile $T_0(z)$. Displacement is the depth offset of the isotherm from $Z_0(T)$ (Desaubies and Gregg 1981):

$$\zeta = z - Z_0(T). \tag{13}$$

We use temperature measurements because the thermistor on Marlin was more stable than the conductivity sensor to long-term drifts. The region was not subject to salinity-compensating intrusions (data from R/P *FLIP*, analyzed by the author, supplied by L. Rainville and R. Pinkel 2006, personal commmunication), and comparisons with density estimates indicate that there was no difficulty with this procedure.

Marlin's motion is discussed in detail in the appendix. At low wavenumbers ($k_x < 10^{-2}$ cpm), Marlin's vertical motion has a red spectrum with a slope much greater than that of the internal waves (approximately k_x^{-4}). At higher wavenumbers, the slope is less steep, but there is much less motion. At wavenumbers $k_x > 10^{-3}$ cpm, both temperature and displacement spectra are more than an order of magnitude greater than this (Fig. 5). A Monte Carlo analysis (appendix) indicates that vertical motions would have to be 10 times what they are to affect the analyses made here.

4. Character of displacement spectra

Example spectra

We present isopycnal slope spectra computed in 5-km bins, each representing approximately 1.4 h of data. Data were discarded when Marlin had a vertical excursion greater than 50 m over the 5 km. To make the spectra more manageable, the time series was low passed and decimated at 20 Hz, or approximately 5-cm horizontal scale. Spectra are presented as wavenumber spectra because Marlin's speed through the water, $c \approx 1 \, m \, s^{-1}$, is faster than all but the lowest-mode internal waves. In deep water, these fast waves have horizontal wavelengths much larger than 5 km and so are not resolved in our spectra.
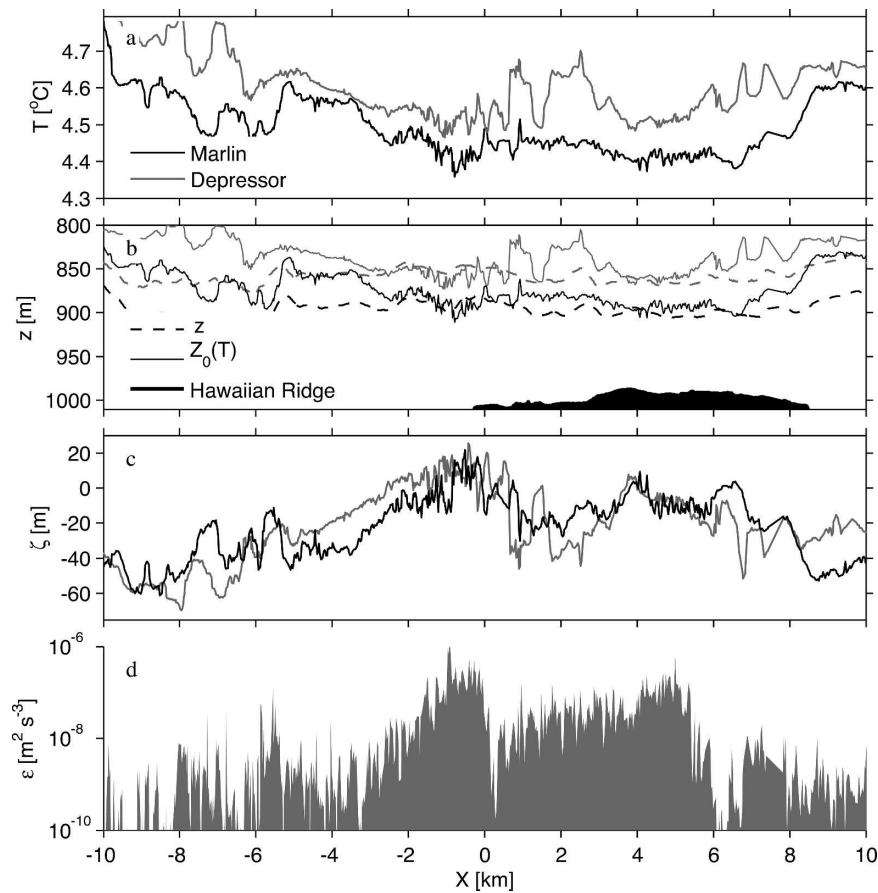
FIG. 4. Example data from a tow over the ridge; data are from 1232 to 1822 UTC 18 Oct 2002. Marlin was moving from left to right in these plots. (a) Temperature signal from Marlin and the depressor; all data are 24-s averages. (b) Marlin and depressor depths (solid); the seafloor is indicated with a thick solid line, and dashed lines show the depth that the temperature measured by each instrument came from an average profile $Z_0(T)$ collected from profilers during the experiment. (c) Isotherm displacements $\zeta = z - Z_0(T)$ for each vehicle; negative values imply that the isotherm is deeper than its average level. (d) Turbulent dissipation rates over the same 24-s windows.

Nine example spectra from three depths and three varying turbulence levels are shown in Fig. 6. The shallow data (Figs. 6a–c) were all collected at depths within 30 m of each other, so the background stratifications are comparable between each example. The first two spectra, with lower dissipations, exhibit a low-wavenumber region where spectra are slightly red and a high-wavenumber region where spectra are distinctly blue. Spectra with the highest turbulence dissipation do not have an obvious red subrange, though it is less blue below 5×10^{-1} cpm. For these examples, the variance at all wavenumbers increases with increasing turbulence. This is a robust feature of the high-wavenumber end of the spectra (Part II).

Spectra from depths near 1800 m (Figs. 6d–f) and near 2400 m (Figs. 6g–i) are remarkably similar in char-acter with all but the most turbulent spectra displaying both low-wavenumber red and high-wavenumber blue portions. The deeper spectra have greater amplitude, in accordance with Eq. (4).

Binning the 5-km spectra by turbulence diffusivity ($K_\rho = 0.2\varepsilon/N^2$) removes the stratification dependence of ε and reveals a systematic variation to the spectra (Fig. 7). The amplitude of the spectra are normalized by N/N_0 [Eq. (4)]. To leading order, this scaling collapses the stratification dependence of the internal waves and remaining amplitude variation should be due to in-creasing energy in the wave field.

At low wavenumbers there is little variation in the amplitude of binned spectra. Internal-wave-based pa-rameterizations of turbulence predict that $K_\rho \sim E^2$ (Henyey et al. 1986; Gregg 1989). If the low-wave-
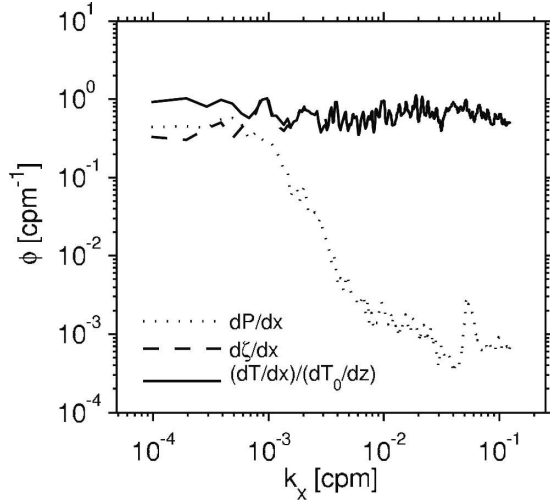
FIG. 5. Gradient spectra of pressure, isopycnal displacement, and temperature scaled by the background temperature gradient computed from data obtained on a long cross-ridge tow. The data come from the full off-ridge tow shown in Fig. 4. The spectrum of $d\zeta/dx$ merges with the scaled temperature gradient spectrum at $k_x \simeq 10^{-3}$ cpm.

number internal wave spectra scaled with E, the three-order-of-magnitude change in K_ρ should have corresponded to a factor-of-30 spread in low-wavenumber amplitudes, not evident in these spectra.

5. Interpretation of spectra

a. High k_x

We interpret the high-wavenumber portion of the spectra presented above as turbulence (Part II; Fig. 8). To interpret the low-wavenumber portion of the spectrum we fit a turbulent model to the high wavenumbers [Eq. (12)] and subtract it from the spectrum, yielding a "corrected" spectrum. Patches with nothing left in the corrected spectrum are not analyzed further.

The wavenumber at which the internal wave subrange transitions to turbulence varies in a predictable manner (Fig. 9) with more energetic turbulence pushing the crossover to lower wavenumbers. For the spectra at 700 m, the crossover is centered about $k_x^c = 10^{-9/2}K_\rho^{-1/2}$, though with considerable variability. These crossover wavenumbers are quite low, implying that horizontal scales in excess of 300 m are affected by the most energetic turbulence. The low-wavenumber extent of the turbulent signature is surprising and is discussed in detail in Part II.

b. Low k_x

Following Garrett–Munk (GM) and previous investigators, the low-wavenumber spectra are fit to a single power law:

$$\phi = ak_x^p \qquad (14)$$

by taking the logarithm and fitting in linear space

$$\log_{10}(\phi) = p \log_{10}(k_x) + \log_{10}(a), \qquad (15)$$

where for the power-law parameter n in the GM formalism [Eq. (8)], $p = 2 - n$, so $p = -0.5$ for GM75, and $p = 0$ for GM81.

Both the uncorrected and corrected spectra were fit over $3.18 \times 10^{-4} < k_x < 2 \times 10^{-2}$ cpm. For corrected spectra, the upper limit of the fit was the crossover wavenumber if $k_x^c < 2 \times 10^{-2}$ cpm. For the uncorrected spectra $p \approx -0.32 \pm 0.3$ (Fig. 10). Conditional sampling on data from different depths does not produce significantly different histograms or means. Corrected spectra are slightly steeper: $p = -0.46 \pm 0.4$. The increase in uncertainty arises because the correction removes spectral information. In terms of the GM formalism, we would assign a power law [Eq. (8)] of $n \approx 2.5$, in agreement with previous horizontal fits (Katz 1975; Katz and Briscoe 1979; Müller et al. 1978).

c. Towed vertical coherence

While the average slope agrees with previous observations, agreement of spectral shape in one dimension does not necessarily imply that internal waves are present in the signal. A consistency check is to consider the coherence between vertically separated Δz sensors:

$$\gamma = \frac{\int\int \cos(k_z \Delta z)\phi(k_x, k_y, k_z) \, dk_y \, dk_z}{\int\int \phi(k_x, k_y, k_z) \, dk_y \, dk_z} . \qquad (16)$$

This was evaluated numerically for a horizontally isotropic GM75 spectrum $\phi(k_x, k_y, k_z)$, where vertical and horizontal components are related by the dispersion relation (Katz and Briscoe 1979).

A depressor weight towed $\Delta z \approx 30$ m above Marlin was equipped with a temperature sensor from which the coherence squared was computed:

$$\gamma^2 = \frac{|\phi_{XY}|^2}{\phi_{XX}\phi_{YY}}, \qquad (17)$$

where ϕ_{XY}, ϕ_{XX}, and ϕ_{YY} are the cospectrum and autospectrum of the isopycnal displacements at Marlin and the depressor. Four depth bins are presented. The data in each depth bin are bootstrap averaged to give an idea of the measurement spread (Fig. 11a). The resulting coherences are consistent with internal waves. Large horizontal wavelengths exhibit more vertical coherence because they are dominated by large vertical
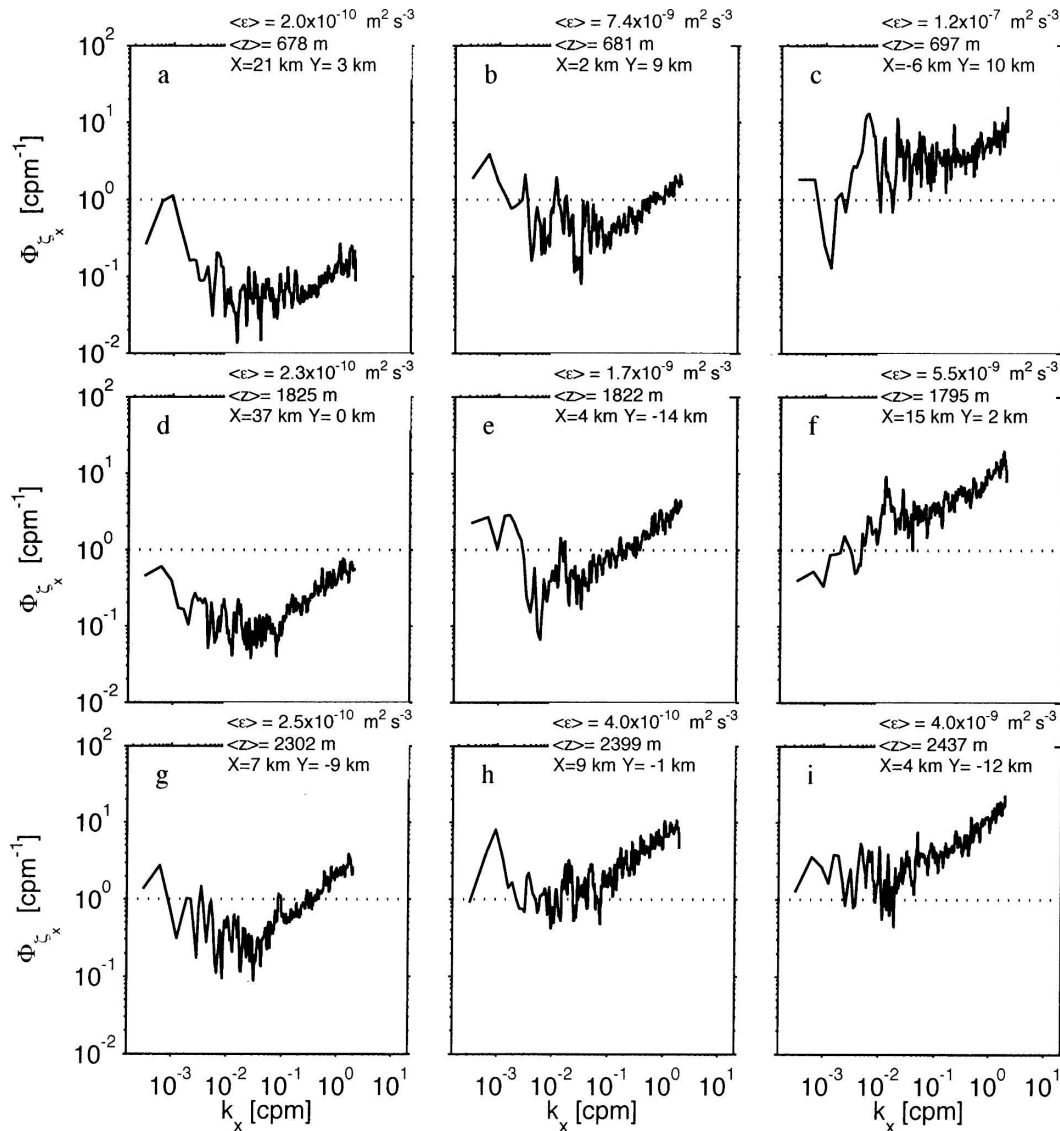
FIG. 6. Example of isopycnal slope spectra: rows show spectra from three increasing depths, and columns represent spectra with increasing turbulence dissipation rates. Spectra have been lightly smoothed geometrically.

wavelength waves. Since stratification decreases with depth, the coherence goes up as vertical scales increase.

A similar coherence was computed between the fin sensor $\Delta z = 1.16$ m below the nose (Fig. 11b). These sensors were a fixed distance apart and yielded a more consistent estimate. The fin sensor data were only usable at $z \approx 700$ m, so we cannot see the change with different stratifications. The coherence is in good agreement with that expected from the GM75 model. This estimate was made on relatively quiescent blocks of data; more turbulent blocks are presented in Part II. We conclude from this that, at large horizontal wavelengths, we are considering motions that have a dispersion relation close to that of internal waves. There are

other low-aspect-ratio motions in the ocean that could lead to similar coherences such as vortical modes (Polzin et al. 2003) or anisotropic turbulence (Gargett 1985; Riley and deBruynKops 2003). However, we are not aware of models for the towed vertical coherence of these motions.

d. Estimating turbulence from horizontal internal wave measurements

We now consider the amplitude of the internal wave spectra and their relation to the turbulence dissipation rate. In the open ocean there is strong evidence that the dissipation is quadratically related to energy in the in-
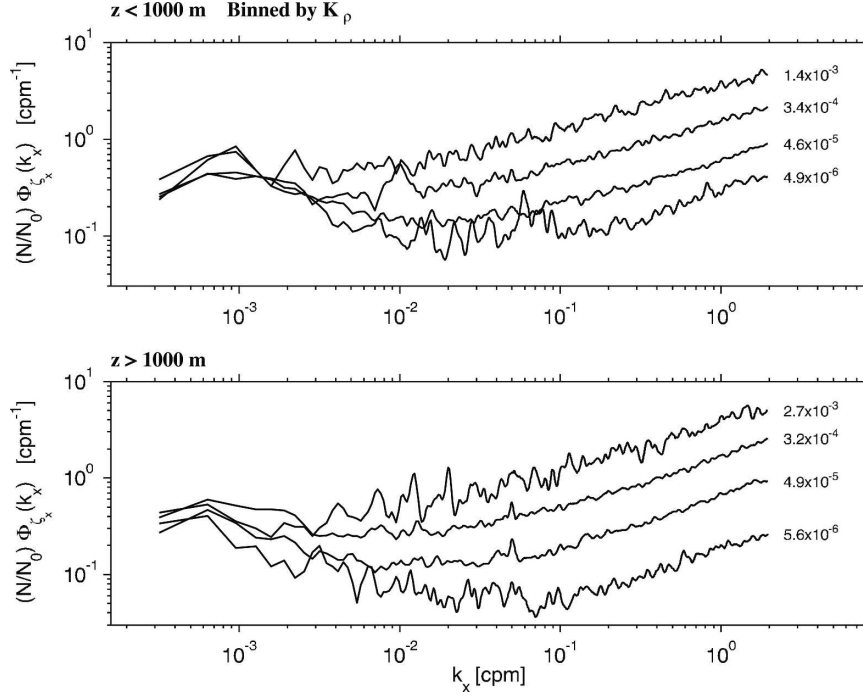
FIG. 7. Average spectra, binned in one-decade bins of K_ρ for shallow and deeper data: spectra have been normalized by their buoyancy frequency.

ternal wave energy (Henyey et al. 1986; Gregg 1989; Gregg et al. 2003):

$$\varepsilon = 7 \times 10^{-10} \frac{N^2}{N_0^2} \frac{E^2}{E_0^2} [\text{m}^2 \text{ s}^{-3}], \qquad (18)$$

where E_0 is the GM81 internal wave energy level. There is evidence from vertical profilers that this parameterization works well at Hawaii (Lee et al. 2006).

We calculate the energy level E in Eq. (18) by dividing the observed spectra by a spectrum with slope $n = 2.5$ and an amplitude in agreement with the GM75 spectrum:

$$E = \left\langle \frac{\phi_{\zeta_x}}{A_0 k_x^{-0.5}} \right\rangle, \qquad (19)$$

where the average is taken over the low-wavenumber portion of the spectrum. The actual value of A_0 is not important as it scales Eq. (18) by an arbitrary factor. The amplitude of the spectra does not strongly correlate to the dissipation rate (Fig. 12a). There is a weak tendency for higher-amplitude spectra to be associated with high dissipation. However, the spread in the estimates is almost as large as the signal, and the correlation coefficient between the log of the quantities is not statistically different from zero. A spatial comparison
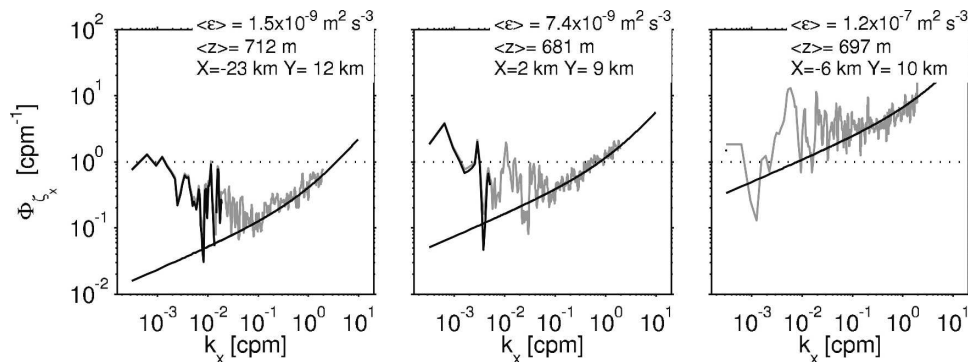

FIG. 8. Three example spectra (as in Figs. 6a–c). A turbulence spectrum [Eq. (2)] is fit (solid curve) to the high-wavenumber range (gray). The internal wave subrange is black.
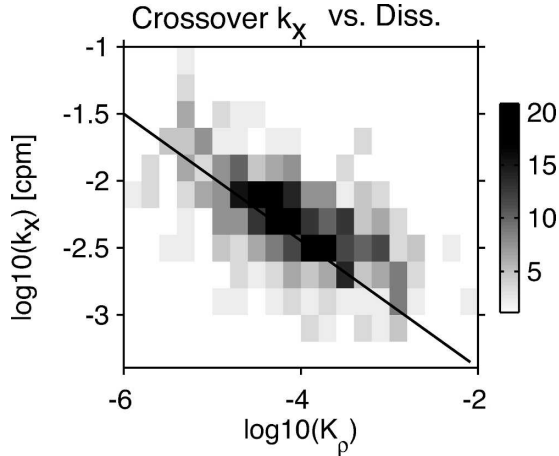
FIG. 9. Value of k_x at which the low-wavenumber portion of the spectra merges with the turbulence. These data are all from 700-m depth.
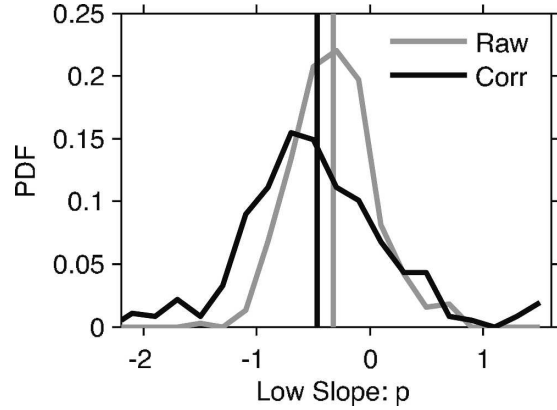

FIG. 10. Slope of low-wavenumber portion of spectra before (gray) and after (black) high-wavenumber spectra are subtracted. For the uncorrected spectra, data are fit out to $k_x = 10^{-2}$ cpm. For the corrected spectra, they are fit as far as there is still a corrected spectrum or to $k_x = 10^{-2}$ cpm, whichever is lower.

across the ridge demonstrates that there is a tendency for the higher amplitude spectra to be found closer to the ridge crest (Fig. 13), in accord with our expectation that there are stronger inernal wave displacements there. However, the uncertainties in this estimate are very large.

This estimate can be contrasted to results from Part II in which the turbulence subrange of the spectra is fit over $0.4 < k_x < 4$ cpm (Fig. 12b). This more direct estimate yields better agreement with the shear probe measurements.

6. Reconciling observed horizontal spectral shapes with observed vertical shapes

Two aspects of this analysis demonstrate clear differences between vertical and horizontal spectra. First, $\phi_{\zeta_x} \sim k_x^{-0.5}$ (Fig. 7) in accord with towed spectra that resulted in GM75, but in disagreement with more recent vertical profiles that resulted in GM81. Second, the amplitude of the slope spectrum does not appear strongly correlated to ε, whereas the amplitudes of strain spectra typically are. Here, we compute slope spectra based on the two-subrange spectral model of strain. Following GM75, we assume that vertical and frequency spectra are separable. However, two vertical subranges means that the horizontal spectrum will not be separable. The horizontal transform convolves the linear and saturated subranges, producing spectra with an intermediate slope and small amplitude variations.

a. Vertical spectra with one subrange

First, for simplicity's sake, we consider a vertical spectrum with only one subrange but four different en-

ergy levels. This demonstrates the effect of transforming a vertical spectrum to horizontal wavenumbers. We choose $E = (1, \sqrt{10}, 10, \sqrt{100})E_0$ to correspond to dissipation rates increasing by three orders of magnitude (as plotted in Fig. 7). Vertical spectra are specified by mode number j, rather than k_z, following Munk (1981). The two are related by the stratification:

$$j = 2bk_z N_0 N^{-1}. \quad (20)$$

The same form for the vertical wavenumber spectrum is used:

$$H(j) = A(j^2 + j_*^2)^{-n/2}, \quad (21)$$

where A is a constant so that $\Sigma_1^{j_{max}} H(j) = 1$. Here we set $j_* = 0$. The dispersion relation is approximated as

$$\omega^2 = \left(\frac{Nb}{\pi j}\right)^2 k_H^2 + f^2. \quad (22)$$

Here we follow GM81 and set $n = 2$ in Eq. (21) and arbitrarily cut the spectra off at a high wavenumber, $j = 2500$, corresponding to a vertical scale of 1 m (Fig. 14a).

The horizontal wavenumber spectrum of $\phi(k_H)$ is calculated from the model spectrum $\phi(j, \omega)$ using the dispersion relation, Eq. (9), and the fact that

$$\phi_{\zeta_x}(k_H) = \sum_{j=1}^{j_{max}} \phi_{\zeta_z}(j,\omega)\frac{d\omega}{dk_H} \quad (23)$$

(Munk 1981): $\phi(j, \omega)$ is given by Eq. (5), where j is used instead of k_z, and from the dispersion relation

$$\frac{d\omega}{dk_H} = \left(\frac{Nb}{\pi j}\right)^2 \frac{k_H}{\omega}. \quad (24)$$

a) Sensor separation: $\Delta z = 40$ m

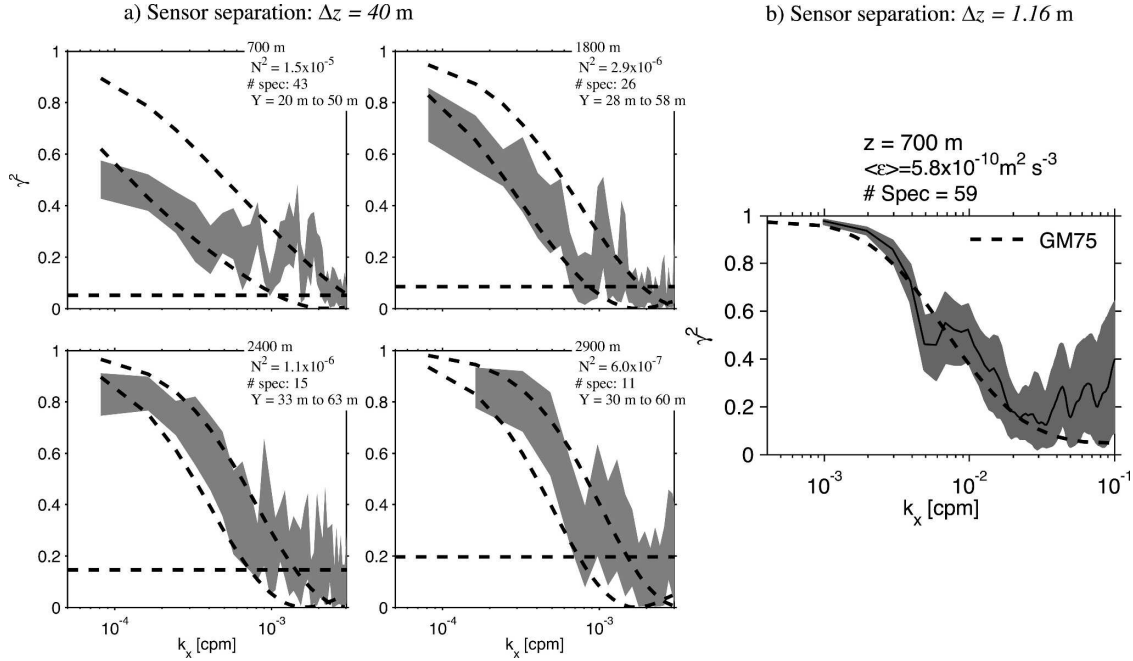b) Sensor separation: $\Delta z = 1.16$ m

FIG. 11. (a) Towed vertical coherence between depressor and Marlin in four depth bins: Data are taken from all data during the cruise. Thick dashed curves are theoretical coherence at separations spanning the observed data separations using the GM75 spectrum (with bandwidth parameter $j_* = 1$; $j_* = 6$ predicts somewhat lower coherences). The horizontal dashed line is the 95% confidence interval for the coherence being different from 0. (b) Towed vertical coherence between the nose and the fin 1.16 m below; these data are from low-dissipation regions at 700-m depth.

This calculation was carried out for three frequency spectra $B(\omega)$ (Fig. 14b): first, a spectrum consisting only of a peak at the tidal frequency M_2; second, the GM81 form [Eq. (7)]; and third, a combination of the two with a peak at M_2, an ω^{-2} slope for $\omega > M_2$, and no slope for $\omega < M_2$. This spectrum is modeled on the frequency spectrum measured by a mooring near the study site (Aucan et al. 2006) and has characteristics similar to those noted by Levine (2002). All three frequency spectra are normalized so that

$$\int_f^N B(\omega)\, d\omega = 1. \qquad (25)$$

For the frequency spectra consisting of a spike at M_2, each value of j has a unique value of k_H, and the k_H spectrum looks just like the k_z spectrum (Fig. 15a). There is some thickness to the low-wavenumber peaks because the frequency spectrum had some width at M_2 for numerical reasons. If we use a broadband frequency spectrum (Fig. 15c), then the discretization at low wavenumbers and the cutoff at high wavenumbers are blurred by applying the dispersion relation. Last, the frequency spectrum with both a peak and some broadband energy produces k_H spectra that exhibit both characteristics (Fig. 15e).

The x-direction spectrum is calculated by noting that $k_H = (k_x^2 + k_y^2)^{1/2}$, assuming that the wave field is isotropic, and integrating in the k_y direction:

$$\phi_{\zeta_x}(k_x) = 2 \int_0^\infty \frac{\phi(k_H)}{2\pi k_H}\, dk_y \qquad (26)$$

(Garrett and Munk 1972). This yields the k_x spectra in Figs. 15b,d,f. They are very similar to k_H spectra, except the features in the spectra are smoothed even more.
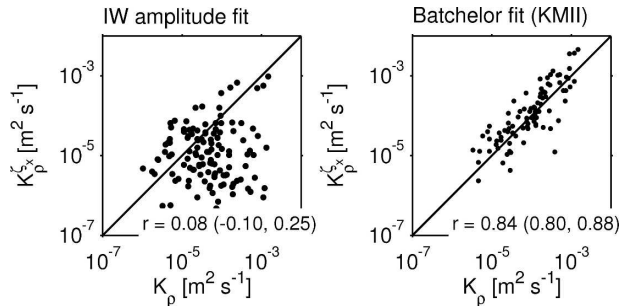

FIG. 12. (a) Comparing the turbulence estimate based on the amplitude of the low-wavenumber slope spectra with the shear probe estimate: the correlation coefficient between these two estimates is shown. (b) Five-kilometer averages of the dissipation estimates made from fitting the high-wavenumber subrange to the Batchelor spectra (described in Part II).
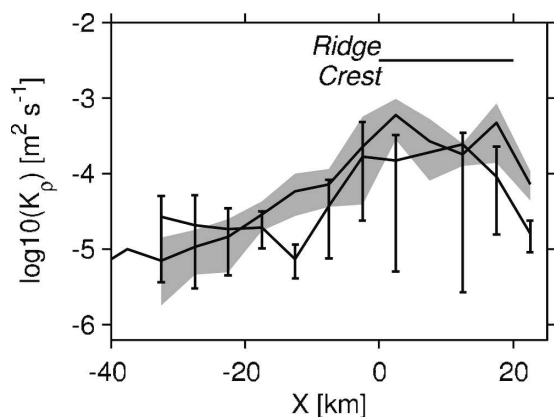
FIG. 13. Comparison of K_ρ in the cross-ridge direction estimated from the shear probes (gray shading) and from the slope spectra [Eq. (18), error bars]. The top of the ridge extends from 0 to approximately 20 km.

When $H(j)$ follows one power law, the horizontal spectra have the same power law except at the highest and lowest wavenumbers. The horizontal spectra also change their amplitude by the same proportion as the vertical spectra.

b. Vertical spectra with two subranges

The same calculation carried out with a two-power-law $H(j)$ yields a richer result. Model spectra are shown in Fig. 16a where, as discussed, the transition from j^0 to j^{-1} moves to lower mode number as the energy of the wave field increases. The same three frequency spectra are used as above.

To compute the horizontal spectra, we assume that the saturated internal waves $j > j_c$ are separable and follow the same dispersion relation as linear internal waves. These are both dubious assumptions. This subrange is still poorly understood (D'Asaro and Lien 2000; Polzin et al. 2003). Lacking further information, we proceed to see where the calculation leads.

The resulting horizontal spectra of a single-frequency wave field look like the vertical spectra (Figs. 17a,b)

with the cutoff wavenumber predicted by the dispersion relation. For a wave field with broad frequency content (Figs. 17c,d), the transition between subranges is spread in horizontal wavenumber. These spectra are curved, with a slightly red slope, but not as steep as k_H^{-1} until the highest wavenumbers. In this subrange, the horizontal spectra are a combination of linear and saturated vertical subranges.

The final case uses the broadband frequency spectrum with an M_2 peak (Figs. 17e,f). The resulting spectra asymptotically approach $\phi_{\zeta_x}(k_x) \sim k_x^0$ at low wavenumbers and $\phi_{\zeta_x}(k_x) \sim k_x^{-1}$ at high. However, they have a broad wavenumber range where $\phi_{\zeta_x}(k_x) \sim k_x^{-0.5}$. In this range, there is only weak variability of the spectral amplitude with energy level.

This last calculation demonstrates why horizontal measurements have a different internal wave spectral shape than vertical measurements. The frequency content of the wave field maps j_c to a spectrum of wavenumbers, k_H, so that the horizontal spectra have a slope intermediate to k^0 and k^{-1}. Calculating the spectra of k_x blurs the transition further. The calculation also demonstrates why we observe a poor correlation of spectral amplitude to ε. Horizontal spectra at the wavenumbers that we measure are largely in the saturated subrange, which varies little as internal wave energy increases. It should be possible to invert and get a vertical spectrum from which we can estimate the energy level. However, this requires knowing $B(\omega)$ and believing that the wave field is isotropic, assumptions that are difficult to measure from a towed instrument. Furthermore, the sensitivity of such a measurement would be much weaker than from a vertical profiler. Estimating the dissipation rate from vertical measurements works so well because ε is proportional to the amplitude of the low vertical wavenumber spectrum squared. The calculations here indicate that the sensitivity is greatly reduced in horizontal measurements.

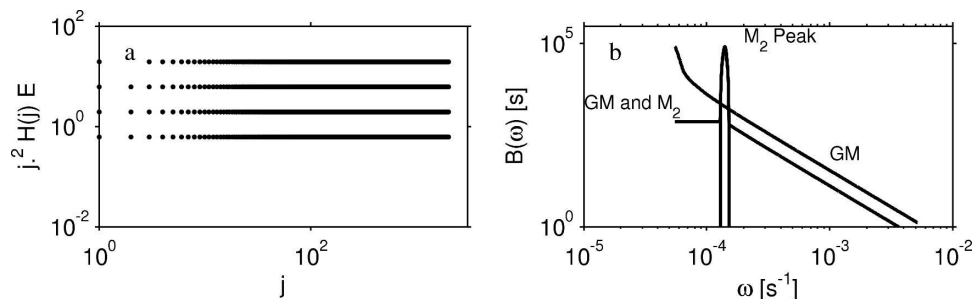The modeled horizontal spectra all decay at low

FIG. 14. (a) The GM81 vertical mode number spectrum $H(j)$, with no saturated subrange: the spectrum is set to 0 for $j > 250$. (b) Three frequency spectra $B(\omega)$.
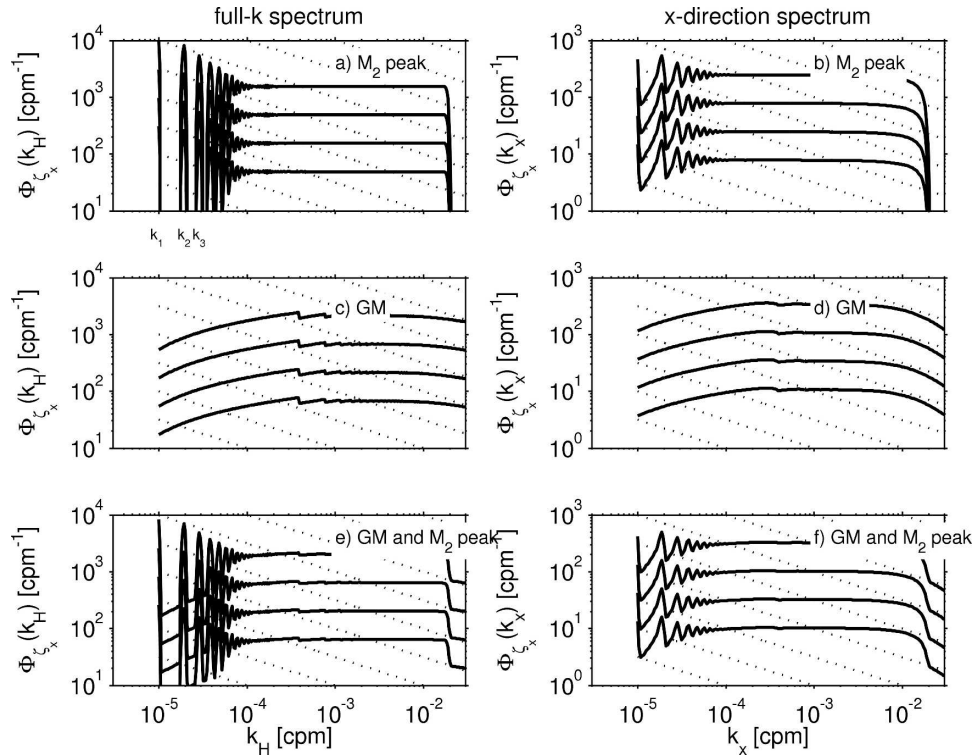
FIG. 15. Horizontal spectrum from a single-subrange GM81 model. Full-horizontal spectrum (k_H) and spectrum in the x direction (k_x) (Fig. 14). Four energy levels are shown. Dashed lines are $k^{-0.5}$ every half decade.

wavenumbers. The spectra were calculated with a gravest vertical mode of $j = 1$, giving a bound on how much energy can exist in the spectra at low wavenumbers. This roll off, and a general whitening of the spectra, occur despite the fact that $j_* = 0$. The whitening would still occur if we had performed the calculation with a continuum of vertical wavenumbers, rather than modes because of the low-k_x asymptote to the linear power law k_x^0. The GM fits to the spectra that incorporate these bandwidth parameters primarily come from horizontal measurements, so they may be unnecessary.

This calculation makes unwarranted assumptions about the linearity and frequency content of the saturated subrange. If the linear dispersion relation is not a good approximation in the saturated subrange or the frequency content is particularly different from the rest of the wave field, this calculation will need to be modified. We do not feel that the model–data agreement is adequate to advocate that these assumptions are accurate. The calculation demonstrates that, in principle, a vertical spectrum composed of two subranges will have a curved power law in the horizontal.
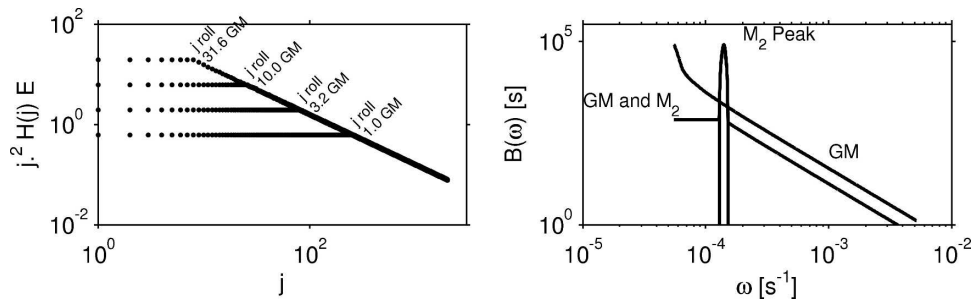

FIG. 16. (a) The GM81 vertical mode number (j) spectrum with a saturated subrange. (b) The three-model frequency spectrum.
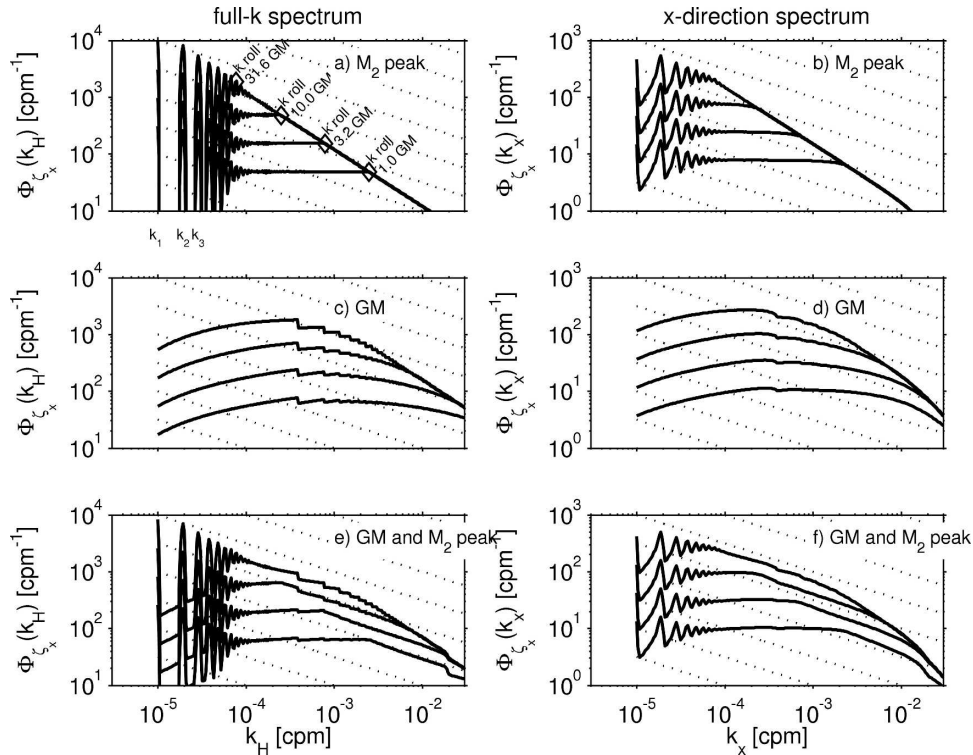
FIG. 17. Full-horizontal spectrum (k_H) and spectrum in the x direction (k_x) calculated from a GM81 model without a saturated subrange (Fig. 16).

7. Summary and discussion

We have presented the first coincident measurements of internal waves and direct turbulence from a horizontal towed vehicle. Our ability to estimate the turbulence dissipation rate and relate internal waves to turbulence intensity is novel. Isopycnal slope spectra results are summarized as follows:

- Low-wavenumber spectra are slightly red ($\phi_{\zeta_x} \sim k_x^{-0.5}$), in agreement with previous towed data (Fig. 10) (GM75) but contrary to vertical measurements, which are usually white at vertical wavenumbers less than 0.1 cpm (GM81), falling off as k_z^{-1} at higher wavenumbers;
- Low-wavenumber motions have vertical coherences consistent with internal waves (Fig. 11) (GM75), though perhaps consistent with other low-aspect-ratio finescale motions.
- The influence of turbulence is greater than that of internal waves on the spectra at wavenumbers as low as 5×10^{-3} cpm (Fig. 9) (Part II);
- Amplitudes of low-wavenumber spectra are only weakly related to the level of the turbulence (Fig. 12).

The measurements presented here are essentially in agreement with previous towed measurements, though

the (lack of) correlation with dissipation measurements has not previously been demonstrated.

The apparent discrepancy between horizontal and vertical measurements is reconciled by including the saturated internal wave subrange in a model of the slope spectrum (section 6). This calculation indicates that the measured wavenumbers include the saturated subrange of internal waves with a frequency-dependent contribution for the linear subrange (Fig. 1b).

Because horizontal spectra are not separable in frequency and wavelength, their interpretation is very difficult. If there were just one power law for all wavenumbers, as was assumed in the early towed work and the GM formalisms, measuring vertically or horizontally would be equivalent. However, having two power laws in the strain spectrum obscures the shape and energy level of the slope spectrum; the transform depends on the frequency content of the waves, which is usually not available from horizontal measurements. In particular, we are not confident that horizontal tows shed much light on the saturated subrange, though it is possible that adding more vertical information could improve this approach.

Horizontal measurements are not the best way to estimate the energy of the internal wave field. Longer tows may resolve horizontal wavenumbers that indicate

the energy level, but this involves averaging over many tens of kilometers. At Hawaii, these scales are larger than the scales at which turbulence decays. The inability to estimate the internal wave energy means that internal wave–based parameterizations cannot easily be used to estimate the turbulence dissipation rate from horizontal measurements. On the other hand, because more of the turbulence spectrum is revealed in horizontal measurements than in vertical, it is possible to fit a turbulence model to finescale measurements of vertical displacements and obtain useful dissipation estimates (Part II).

APPENDIX

Importance of Errors in the Displacement Calculation

Horizontal spectra have been measured from vehicles that do not undulate on the horizontal scales of interest (Katz 1975; McKean and Ewart 1974). Marlin does move up and down raising the concern that it aliases horizontal spectra by including vertical variations. Performing the spectra on displacement rather than temperature removes some of this added variance (Fig. 4c). However, it is not clear beforehand whether there is still significant aliasing.

A second effect that should be considered is errors induced by the finite tow speed. The horizontal spectra assume that the tow is made much faster than the observed wave speeds. This is not true for the lowest-mode waves in the system. How that affects our results is an important question. Monte Carlo internal wave simulations show that the error is not significant for a GM wave field.

If Marlin moves with velocity (u, w), then the rate of change of the displacement observed is
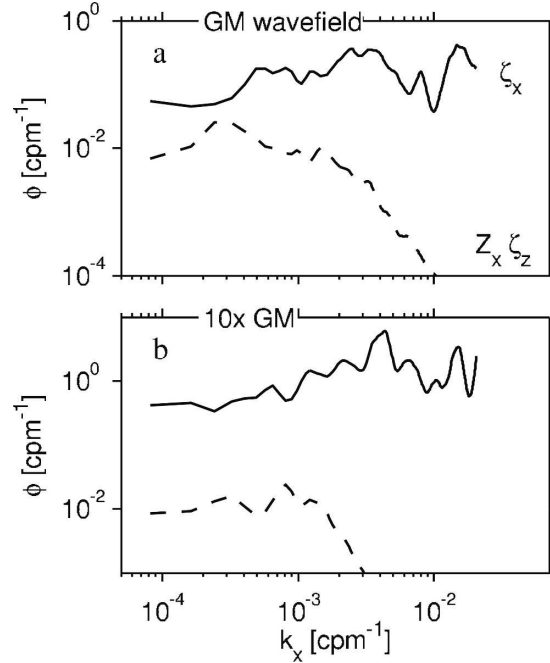

FIG. A1. Comparison of simulated internal wave displacement spectrum and the signal induced by the instrument moving with a path given by $\partial Z/\partial x$, through the simulated strain field ζ_x: (a) for a GM wave field and (b) for a GM-shaped wave field with 10 times the energy.

$$\frac{\partial \zeta}{\partial t} = u \frac{\partial \zeta}{\partial x} + w \frac{\partial \zeta}{\partial z}. \qquad (A1)$$

We can rewrite this as

$$\frac{\partial \zeta'}{\partial x} = \frac{\partial \zeta}{\partial x} + \frac{dZ}{dx} \frac{\partial \zeta}{\partial z}, \qquad (A2)$$

where $\partial \zeta'/\partial x = u^{-1}\partial \zeta/\partial t$ is measured as the horizontal derivative of the displacement. $dZ/dx = w/u$ is the horizontal derivative of Marlin's vertical motion. In order for Marlin to be a good means of measuring the horizontal spectrum of displacement

$$\frac{\partial \zeta}{\partial x} \gg \frac{dZ}{dx} \frac{\partial \zeta}{\partial z}. \qquad (A3)$$

In terms of spectra, this can be written as

$$\phi(\zeta_x) \gg \phi(Z_x \partial \zeta/\partial z). \qquad (A4)$$

A method for calculating a GM81 wave field is presented by Sun and Kunze (1999). For the data presented here, 100 000 waves were picked randomly from (ω, j) that corresponds to the GM75 spectra. The horizontal direction and phase of each wave were chosen randomly. The amplitude and probability of a certain mode number and frequency for each wave was chosen to reproduce the GM75 spectrum. Note, however, that
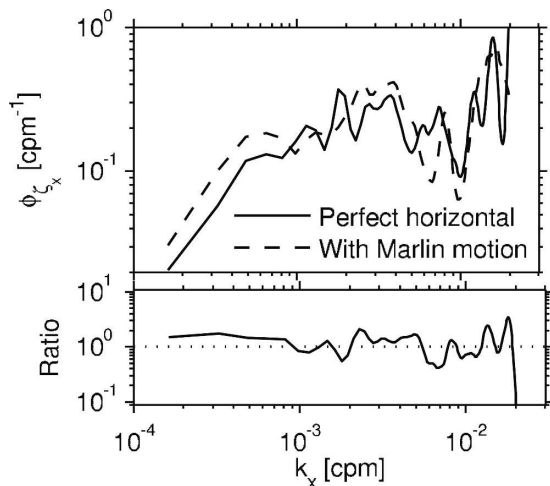
FIG. A2. Horizontal spectra of ζ_x for a perfect instrument (solid) and for a Marlin tow (dashed).

we did not implement a j^{-1} roll off in the mode number spectrum. We assumed an instrument at the GM stratification $N = N_{GM}$; smaller stratifications have larger vertical scales, so the errors considered here become smaller.

This wave field was then sampled for a perfect instrument ($dZ/dx = 0$ and $u = \infty$) and for a sample path. A comparison of the two spectra in Eq. (A4) demonstrates that for the observed motion, $\phi(\zeta_x)$ exceeds $\phi(Z_x\zeta_x)$ by almost an order of magnitude (Fig. A1a). For a wave field with 10 times the energy, the error term is almost an order of magnitude smaller than the signal (Fig. A1b).

This comparison is borne out by considering the observed quantities themselves (Fig. A2). There is no systematic difference between the spectrum and that measured by the synthesized Marlin. Even increasing Marlin's vertical displacements by a factor of 20 only causes a factor-of-2 increase in the measured spectrum. This analysis indicates that Marlin's motions do not strongly alias internal wave motions.

REFERENCES

Alford, M. H., and M. C. Gregg, 2001: Near-inertial mixing: Modulation of shear, strain and microstructure at low latitude. *J. Geophys. Res.,* **106,** 16 947–16 968.

Aucan, J., M. A. Merrifield, D. S. Luther, and P. Flament, 2006: Tidal mixing events on the deep flanks of Kaena Ridge, Hawaii. *J. Phys. Oceanogr.,* **36,** 1202–1219.

Batchelor, G. K., 1959: Small-scale variation of convected quantitites like temperature in turbulent fluid. *J. Fluid Mech.,* **5,** 113–139.

Cairns, J. L., and G. O. Williams, 1976: Internal wave observations from a midwater float, II. *J. Geophys. Res.,* **81,** 1943–1950.

D'Asaro, E. A., 1995: Upper-ocean inertial currents forced by a strong storm. Part II: Modeling. *J. Phys. Oceanogr.,* **25,** 2937–2952.

——, and R.-C. Lien, 2000: The wave-turbulence transition for stratified flows. *J. Phys. Oceanogr.,* **30,** 1669–1678.

Desaubies, Y. J. F., and M. C. Gregg, 1981: Reversible and irreversible finestructure. *J. Phys. Oceanogr.,* **11,** 541–556.

Dugan, J. P., W. D. Morris, and B. S. Okawa, 1986: Horizontal wave number distribution of potential energy in the ocean. *J. Geophys. Res.,* **91,** 12 993–13 000.

Gardner, C. S., 1996: Testing theories of atmospheric gravity wave saturation and dissipation. *J. Atmos. Terr. Phys.,* **58,** 1575–1589.

Gargett, A. E., 1985: Evolution of scalar spectra with the decay of turbulence in a stratified fluid. *J. Fluid Mech.,* **159,** 379–407.

——, P. J. Hendricks, T. B. Sanford, T. R. Osborn, and A. J. Williams III, 1981: A composite spectrum of vertical shear in the upper ocean. *J. Phys. Oceanogr.,* **11,** 1258–1271.

Garrett, C., and W. Munk, 1972: Space-time scales of internal waves. *Geophys. Fluid Dyn.,* **2,** 225–264.

——, and W. H. Munk, 1975: Space-time scales of internal waves: A progress report. *J. Geophys. Res.,* **80,** 291–297.

Gregg, M. C., 1989: Scaling turbulent dissipation in the thermocline. *J. Geophys. Res.,* **94,** 9686–9698.

——, and E. Kunze, 1991: Shear and strain in Santa Monica Basin. *J. Geophys. Res.,* **96,** 16 709–16 719.

——, E. A. D'Asaro, T. J. Shay, and N. Larson, 1986: Observations of persistent mixing and near-inertial waves. *J. Phys. Oceanogr.,* **16,** 856–885.

——, D. Winkel, and T. Sanford, 1993: Varieties of fully resolved spectra of vertical shear. *J. Phys. Oceanogr.,* **23,** 124–141.

——, T. B. Sanford, and D. P. Winkel, 2003: Reduced mixing from the breaking of internal waves in equatorial waters. *Nature,* **422,** 513–515.

Hebert, D., and J. Moum, 1994: Decay of a near-inertial wave. *J. Phys. Oceanogr.,* **24,** 2334–2351.

Henyey, F. S., J. Wright, and S. M. Flatté, 1986: Energy and action flow through the internal wave field. *J. Geophys. Res.,* **91,** 8487–8495.

Hines, C. O., 1991a: The saturation of gravity waves in the middle atmosphere. Part I: Critique of linear-instability theory. *J. Atmos. Sci.,* **48,** 1348–1360.

——, 1991b: The saturation of gravity waves in the middle atmosphere. Part II: Development of Doppler-spread theory. *J. Atmos. Sci.,* **48,** 1360–1379.

Katz, E. J., 1975: Tow spectra from Mode. *J. Geophys. Res.,* **80,** 1163–1167.

——, and M. G. Briscoe, 1979: Vertical coherence of the internal wave field from towed sensors. *J. Phys. Oceanogr.,* **9,** 518–530.

Klymak, J. M., and J. N. Moum, 2007: Oceanic isopycnal slope spectra. Part II: Turbulence. *J. Phys. Oceanogr.,* **37,** 1232–1245.

——, and Coauthors, 2006: An estimate of tidal energy lost to turbulence at the Hawaiian Ridge. *J. Phys. Oceanogr.,* **36,** 1148–1164.

Kunze, E., and T. B. Sanford, 1996: Abyssal mixing: Where it is not. *J. Phys. Oceanogr.,* **26,** 2286–2296.

——, E. Firing, J. M. Hummon, T. K. Chereskin, and A. M. Thurnherr, 2006: Global abyssal mixing inferred from lowered ADCP shear and CTD strain profiles. *J. Phys. Oceanogr.,* **36,** 1553–1576.

Lee, C. M., E. Kunze, T. B. Sanford, J. D. Nash, M. A. Merrifield,

and P. E. Holloway, 2006: Internal tides and turbulence along the 3000-m isobath of the Hawaiian Ridge. *J. Phys. Oceanogr.,* **36,** 1165–1183.

Levine, E. R., and R. G. Lueck, 1999: Turbulence measurements with an autonomous underwater vehicle. *J. Atmos. Oceanic Technol.,* **16,** 1533–1544.

Levine, M. D., 2002: A modification of the Garrett–Munk internal wave spectrum. *J. Phys. Oceanogr.,* **32,** 3166–3181.

McKean, R.S., and T.E. Ewart, 1974: Temperature spectra in the deep ocean off Hawaii. *J. Phys. Oceanogr.,* **4,** 191–199.

Moum, J. N., M. C. Gregg, R. C. Lien, and M. Carr, 1995: Comparison of turbulence kinetic energy dissipation rate estimates from two ocean microstructure profilers. *J. Atmos. Oceanic Technol.,* **12,** 346–366.

——, D. R. Caldwell, J. D. Nash, and G. D. Gunderson, 2002: Observations of boundary mixing over the continental slope. *J. Phys. Oceanogr.,* **32,** 2113–2130.

Mudge, T. D., and R. G. Lueck, 1994: Digital signal processing to enhance oceanographic observations. *J. Atmos. Oceanic Technol.,* **11,** 825–836.

Müller, P., D. J. Olbers, and J. Willebrand, 1978: The IWEX spectrum. *J. Geophys. Res.,* **83,** 479–500.

Munk, W. H., 1981: Internal waves and small-scale processes. *Evolution of Physical Oceanography,* B. A. Warren and C. Wunsch, Eds., MIT Press, 264–291.

Nagasawa, M., T. Hibiya, Y. Niwa, M. Watanabe, Y. Isoda, S. Takagi, and Y. Kamei, 2002: Distribution of fine-scale shear in the deep waters of the North Pacific obtained using ex-pendable current profilers. *J. Geophys. Res.,* **107,** 3221, doi:10.1029/2002JC001376.

Naveira Garabato, A. C., K. I. C. Oliver, A. J. Watson, and M.-J. Messias, 2004: Turbulent diapycnal mixing in the Nordic seas. *J. Geophys. Res.,* **109,** C1201, doi:10.1029/2004JC002411.

Polzin, K. L., 2004: A heuristic description of internal wave dynamics. *J. Phys. Oceanogr.,* **34,** 214–230.

——, J. M. Toole, and R. W. Schmitt, 1995: Finescale parameterizations of turbulent dissipation. *J. Phys. Oceanogr.,* **25,** 306–328.

——, E. Kunze, J. Toole, and R. Schmitt, 2003: The partition of finescale energy into internal waves and subinertial motions. *J. Phys. Oceanogr.,* **33,** 234–248.

Riley, J. J., and S. M. deBruynKops, 2003: Dynamics of turbulence strongly influenced by buoyancy. *Phys. Fluids,* **15,** 2047–2059.

Rudnick, D. L., and Coauthors, 2003: From tides to mixing along the Hawaiian Ridge. *Science,* **301,** 355–357.

Sherman, J. T., and R. Pinkel, 1991: Estimates of the vertical wavenumber–frequency spectra of vertical shear and strain. *J. Phys. Oceanogr.,* **21,** 292–303.

Smith, S. A., D. C. Fritts, and T. E. VanZandt, 1987: Evidence for a saturated spectrum of atmospheric gravity waves. *J. Atmos. Sci.,* **44,** 1404–1410.

St. Laurent, L., and C. Garrett, 2002: The role of internal tides in mixing the deep ocean. *J. Phys. Oceanogr.,* **32,** 2882–2899.

Sun, H., and E. Kunze, 1999: Internal wave–wave interactions. Part I: The role of internal wave vertical divergence. *J. Phys. Oceanogr.,* **29,** 2886–2904.